

Microwave response of fractional quantum Hall droplets with quasiparticle tunneling

Fumihiko Murabayashi,^{1,*} Ryotaro Sano,¹ Flavio Ronetti,² Jérôme Rech,² Thierry Martin,² Thibaut Jonckheere,² and Takeo Kato¹

¹*Institute for Solid State Physics, University of Tokyo, Kashiwa 277-8581, Japan*

²*Aix Marseille Univ, Université de Toulon, CNRS, CPT, Marseille, France*

We theoretically study microwave absorption spectroscopy of fractional quantum Hall droplets in the presence of quasiparticle tunneling across a quantum point contact. This contact-free probe provides access to collective edge dynamics beyond conventional transport measurements. We develop a nonperturbative path-integral Monte Carlo approach that enables computation of the frequency-dependent response at finite temperature and for arbitrary droplet geometries, and benchmark the method against analytical results in the weak-tunneling regime. We find that tunneling produces measurable shifts and broadening of resonance peaks, with systematic dependence on tunneling strength and device geometry. Such shifts and broadenings are not obtained in perturbative treatments acting directly on the response function, but emerge when interaction-kernel effects are properly incorporated. Our results indicate experimentally accessible signatures of edge-mode interference and tunneling-induced renormalization of collective excitations, and support the use of microwave spectroscopy as a quantitative probe of quasiparticle dynamics in mesoscopic quantum Hall structures.

I. INTRODUCTION

Since its discovery in 1982, the fractional quantum Hall effect (FQHE) has had a profound impact on condensed matter physics [1]. Its essence lies in the formation of an incompressible quantum liquid driven by strong electron-electron interactions, and the remarkable agreement between theory and experiment, most notably exemplified by the Laughlin wave function [2], has greatly advanced our understanding of strongly correlated electronic phases. Moreover, the FQHE represents the first clear example of topological order that cannot be characterized by any local order parameter, and it has played a decisive role in establishing fundamental concepts in modern topological materials science.

In recent years, renewed attention has been directed toward quasiparticle excitations in FQH systems. For the Laughlin state realized at filling $\nu = 1/(2m + 1)$ ($m \in \mathbb{Z}$), characterized by a single chiral edge mode encircling the bulk [3], the elementary excitations carry fractional charge. A prominent example is the $\nu = 1/3$ state, in which the quasiparticle contributing to edge transport has been experimentally observed to possess charge $e/3$, as revealed by shot-noise measurements [4, 5]. These quasiparticles are known to be Abelian anyons exhibiting exotic fractional statistics, whereby the many-body wave function acquires a phase factor upon exchanging two particles [6–8]. Thanks to significant advances in nanofabrication and measurement technology, this fractional statistics has recently been directly verified through Fabry–Pérot interferometry and nonequilibrium noise measurements [9, 10]. Motivated by these achievements, both theoretical and experimental studies on anyonic statistics in FQH systems have intensified

rapidly relying either on interferometry [11–15] or time-domain braiding [16–30].

However, most previous studies have focused on transport properties such as current and nonequilibrium noise in devices where a quantum point contact (QPC) or an interferometer is fabricated in the edge channel [31, 32]. Such setups necessarily require attaching source and drain electrodes, making it impossible to avoid the influence of the measurement apparatus itself, including contact resistance and potential fluctuations near the electrodes, on the intrinsic edge structure. Against this background, probing edge excitations via microwave absorption in an isolated quantum Hall droplet [33–35] provides a fundamentally new experimental window distinct from conventional transport measurements [36–44]. In particular, the setup proposed in Ref. [45] capacitively couples a mesoscopic quantum Hall droplet to a microwave waveguide, allowing direct access to the excitation spectrum of edge modes without any Ohmic contacts. This noninvasive feature effectively eliminates contact-induced disturbances, offering a decisive advantage over transport-based approaches. Furthermore, this method offers several additional benefits that are difficult to realize in transport experiments. First, the resonance frequencies of absorption peaks directly encode the propagation velocity of edge modes, while the number of peaks reflects the number of modes, allowing their physical properties to be determined in a highly direct manner. Second, the set of resonance peaks shows a distinctive dependence on the droplet’s shape, offering a way to explore the geometry of the quantum Hall effect [46]. Finally, when multiple edges are present, by simply varying the droplet size, one can effectively cross the equilibration length of the edge, thereby accessing both the equilibrated regime (single peak) and the nonequilibrated regime (multiple peaks) within the same device [45]. This stands in sharp contrast to transport measurements, where accessing different regimes typically requires alter-

* fumihiko@issp.u-tokyo.ac.jp

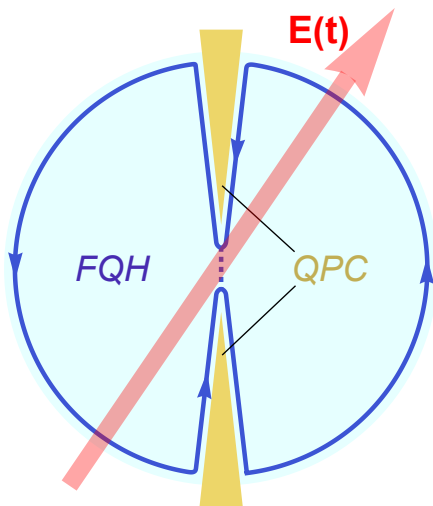


FIG. 1. Schematic view of the setup: a fractional quantum Hall (FQH) droplet with a chiral edge state (blue line) containing a quantum point contact (yellow), allowing tunneling of fractional quasiparticles. The droplet is driven by a time-varying microwave electric field (large red arrow), assumed spatially uniform over the droplet scale.

ing the positions of electrical contacts [47, 48].

In addition, when a QPC is introduced, the absorption peak amplitude exhibits a characteristic interference effect that is linear in the tunneling amplitude, in contrast to the quadratic dependence observed in standard Fabry–Pérot interferometers. This feature greatly enhances sensitivity to quasiparticle charge and statistics. Moreover, contributions from the bulk have frequency and magnetic-field dependences distinct from those of the edge [49, 50], enabling high-precision extraction of pure edge physics from the absorption spectrum.

In this work, we investigate how quasiparticle tunneling through a QPC modifies the microwave absorption spectrum of a FQH droplet as shown in Fig. 1. We compute the finite-temperature response nonperturbatively using path-integral Monte Carlo (PIMC), which treats interactions, thermal fluctuations, and tunneling processes on equal footing and allows access to arbitrary droplet geometries. To gain analytical insight, we complement the numerics with perturbative calculations in the tunneling amplitude for an idealized circular geometry and compare the results. Benchmarking against the exact solution for an integer quantum Hall droplet at $\nu = 1$ demonstrates the consistency of both the analytical framework and numerical implementation. This combined analysis shows that tunneling strength and temperature induce systematic resonance-peak shifts and linewidth broadening. In particular, the peak shifts arise beyond perturbative treatments acting directly on the response function [45], underscoring the importance of taking the interaction kernel into account in discussing the microwave response. Throughout this paper, we set $\hbar = 1$.

II. MODEL AND FORMULATION

A. Bosonization

We consider a circular fractional quantum Hall (FQH) state at a finite temperature T (see Fig. 1), hereafter referred to as a FQH droplet. Such a droplet can be realized by applying a negative voltage to appropriately shaped gate electrodes in a two-dimensional electron system. Owing to the bulk energy gap, all low-energy excitations are confined to the boundary and appear as a single unidirectional chiral edge mode, as indicated by the blue line in Fig. 1. Although this edge mode is described by the chiral Luttinger liquid theory [51, 52], a careful treatment is required for finite-size systems [53, 54].

We introduce a coordinate s along the edge of the FQH droplet and define the edge-state region as $0 \leq s < L$, where L denotes the circumference. In the bosonization method, the normal-ordered electron density $\rho(s)$ is described with a bosonic field as

$$\rho(s) = \frac{1}{2\pi} \partial_s \varphi(s), \quad (1)$$

where $\varphi(s)$ is a bosonic field obeying the commutation relation

$$[\varphi(s), \varphi(s')] = i\pi\nu \operatorname{sgn}(s - s'), \quad (0 < s, s' < L). \quad (2)$$

For a finite system, this bosonic field can be decomposed into two contributions [53, 55]:

$$\varphi(s) = \varphi_0(s) + \varphi_p(s), \quad (3)$$

$$\varphi_0(s) = -\nu\vartheta + \frac{2\pi Ns}{L}, \quad (4)$$

$$\varphi_p(s) = \sum_{k>0} \sqrt{\frac{2\pi\nu}{kL}} \left(b_k e^{iks} + b_k^\dagger e^{-iks} \right) e^{-k\alpha/2}, \quad (5)$$

where $\varphi_0(s)$ and $\varphi_p(s)$ respectively denote the zero mode and the periodic part, $N = \int_0^L ds \rho(s)$ is the charge operator, ϑ is its conjugate phase operator, and b_k^\dagger (b_k) are bosonic creation (annihilation) operators. The summation runs over discrete wave numbers $k = 2\pi n/L$, with n a positive integer. The canonical commutation relation $[\vartheta, N] = i$ holds by construction.

The quasiparticle annihilation operator is described with the bosonic field as [54]

$$\begin{aligned} \psi_q(s) &= \frac{1}{\sqrt{2\pi\alpha}} e^{-i\nu\vartheta} e^{2\pi i Ns/L} e^{i\varphi_p(s)} \\ &= \frac{1}{\sqrt{2\pi\alpha}} e^{i\varphi_0(s) + i\pi\nu s/L} e^{i\varphi_p(s)}, \end{aligned} \quad (6)$$

where α is a short-distance cutoff. In the second equality, the operators have been rearranged using the Baker–Campbell–Hausdorff (BCH) formula [56]. The resulting c -number phase factor $e^{i\pi\nu s/L}$ originates from the non-commutativity of ϑ and N .

The Hamiltonian of the chiral edge mode is given by [54]

$$H = \frac{\pi v}{\nu L} [N^2 + (\phi_{\text{AB}}/\pi + \nu)N] + \sum_{k>0} v k b_k^\dagger b_k, \quad (7)$$

where v is the velocity of the chiral mode. Here we have introduced the Aharonov–Bohm (AB) phase $\phi_{\text{AB}} = 2\pi\Phi/\Phi_0$, where Φ is the magnetic flux through the droplet, and $\Phi_0 = h/e^*$ is the flux quantum corresponding to the quasiparticle charge $e^* = \nu e$. In the presence of the AB phase, the quasiparticle operator is replaced as

$$\psi_{\text{q}}(s) = \frac{1}{\sqrt{2\pi\alpha}} e^{i\varphi_0(s) + i\phi_{\text{AB}}s/L + i\pi\nu s/L} e^{i\varphi_{\text{p}}(s)}. \quad (8)$$

In this work, we only consider the $N = 0$ sector. This is justified when the effect of thermal fluctuations on the charge number N can be neglected. To this end, we consider the low temperature regime ($k_{\text{B}}T \ll 2\pi v/L$), and choose a phase ϕ_{AB} close to $-\pi\nu$ where the thermal fluctuations of N are minimized. Furthermore, the phase operator ϑ can be dropped as we consider quasiparticle tunneling within a single edge mode, which does not modify the total number of quasiparticles on the edge. Therefore, the quasiparticle annihilation operator is simplified as

$$\psi_{\text{q}}(s) = \frac{1}{\sqrt{2\pi\alpha}} e^{i\varphi_{\text{p}}(s)}. \quad (9)$$

In what follows, we denote $\varphi_{\text{p}}(s)$ as $\varphi(s)$ to keep the notations as simple as possible.

B. Effective action

In the following, we derive the effective action by applying the path-integral formalism to the nonzero mode. The imaginary-time action of the edge modes is given as follows: [57]

$$S_{\text{edge}}[\varphi] = \frac{1}{4\pi\nu} \int_0^L ds \int_0^\beta d\tau \partial_s \varphi (i\partial_\tau \varphi + v\partial_s \varphi), \quad (10)$$

where L is the circumference of the circular FQH droplet, and $\beta = 1/k_{\text{B}}T$ is the inverse temperature.

Next, we consider the effect of quasiparticle tunneling at a quantum point contact (QPC). In this study, we focus on quasiparticle tunneling between positions s_1 and s_2 along the edge of the droplet. For a tunneling amplitude λ_r , the action describing the quasiparticle tunneling is given by

$$\begin{aligned} S_{\text{tunn}}[\varphi] &= -\lambda_r \int_0^\beta d\tau [\psi_{\text{q}}^\dagger(s_2, \tau) \psi_{\text{q}}(s_1, \tau) + \text{H.c.}] \\ &= -V \int_0^\beta d\tau \cos[\varphi(s_1, \tau) - \varphi(s_2, \tau)], \end{aligned} \quad (11)$$

where in the last step we set $V = \lambda_r/\pi\alpha$. From this, the action of the system is $S_{\text{edge}}[\varphi] + S_{\text{tunn}}[\varphi]$, and the partition function is expressed using path integrals as

$$Z \propto \int \mathcal{D}\varphi e^{-S_{\text{edge}}[\varphi] - S_{\text{tunn}}[\varphi]}. \quad (12)$$

For the calculation of the response function, we employ the generating functional with an auxiliary real field $\lambda(\tau)$, which allows us to carry out the Gaussian integration everywhere except at the positions s_1 and s_2 :

$$Z \propto \int \mathcal{D}\varphi \mathcal{D}\lambda \mathcal{D}\phi e^{-S_{\text{edge}}[\varphi] - S_{\text{tunn}}[\varphi] - S_\lambda[\varphi, \lambda, \phi]}, \quad (13)$$

where we introduced the action involving the newly defined fields

$$S_\lambda[\varphi, \lambda, \phi] = i \int_0^\beta d\tau \lambda(\tau) [\varphi(s_1, \tau) - \varphi(s_2, \tau) - \phi(\tau)]. \quad (14)$$

Here, $S_\lambda[\varphi, \lambda, \phi]$ enforces the constraint between the fields at s_1 and s_2 .

After performing a Fourier transform, completing the square, and carrying out Gaussian integrations over the fields λ and φ , the generating functional reduces to an action depending only on the local field $\phi(\tau)$, which corresponds to the effective action $S_{\text{eff}}[\phi]$ of the system:

$$Z \propto \int \mathcal{D}\phi e^{-S_{\text{eff}}[\phi]}, \quad (15)$$

$$S_{\text{eff}}[\phi] = S_0[\phi] + S_{\text{tunn}}[\phi]. \quad (16)$$

Here, $S_0[\phi]$ and $S_{\text{tunn}}[\phi]$ represent the contributions from the edge states and quasiparticle tunneling, respectively, and are given by

$$S_0[\phi] = \sum_{\omega_n} \frac{|\phi_n|^2}{4\beta\Lambda_n}, \quad (17)$$

$$S_{\text{tunn}}[\phi] = -V \int_0^\beta d\tau \cos[\phi(\tau)]. \quad (18)$$

Here, ϕ_n is a Fourier transformation of $\phi(\tau)$:

$$\phi(\tau) = \frac{1}{\beta} \sum_{\omega_n} \phi_n e^{-i\omega_n \tau}, \quad (19)$$

and $\omega_n \equiv 2\pi n/\beta$ denotes the bosonic Matsubara frequencies. Λ_n is a function dependent on s_1 and s_2 , which is given by

$$\Lambda_n = \frac{2\pi\nu}{\omega_n} \frac{\sinh\left(\frac{\omega_n|s_1-s_2|}{2v}\right) \sinh\left(\frac{\omega_n(L-|s_1-s_2|)}{2v}\right)}{\sinh\left(\frac{\omega_n L}{2v}\right)}. \quad (20)$$

For a detailed derivation, see Appendix A. One readily sees from Eq. (17) that Λ_n is directly related to the propagator of the effective bosonic field ϕ .

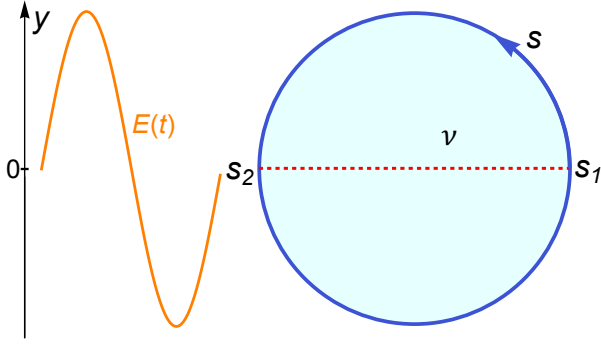


FIG. 2. Schematic of a quantum Hall droplet with circular geometry at filling ν . The coordinate y is defined parallel to the oscillating microwave electric field, while the coordinate s parametrizes the circumference of the droplet. The points s_1 and s_2 denote the positions of the QPCs. Although a realistic droplet would exhibit constrictions at these locations, we consider an idealized setup in which the droplet remains circular and particle (or quasiparticle) tunneling occurs at s_1 and s_2 .

C. Response function

To formulate the microwave response function of the droplet, we first define the polarization of the edge states as follows

$$\hat{P} = \int_0^L ds y(s) \rho(s), \quad (21)$$

where $y(s)$ denotes the y -coordinate of the edge of the droplet, along which the direction of the oscillating electric field is aligned. We assume that the microwave has a sufficiently long wavelength so that the electric field remains constant over the scale of the droplet.

In this work, we focus on an idealized setup in which the droplet remains circular and particle (or quasiparticle) tunneling occurs at s_1 and s_2 , as shown in Fig. 2, serving as a representative example. For a circular droplet with circumference L , $y(s)$ is given by

$$y(s) = \frac{L}{2\pi} \sin\left(\frac{2\pi s}{L}\right). \quad (22)$$

In the rest of this section, we formulate the microwave response for this setup, whereas the extension to different geometries can be carried out analogously and will be discussed in Sec. V.

The Hamiltonian describing the interaction between the microwave electric field and the edge states is then given by

$$\hat{H}^{(\text{ex})}(t) = -E(t)\hat{P} = -E(t) \int_0^L ds y(s) \rho(s). \quad (23)$$

We define the expectation value of the polarization change due to the external field $E(t)$ as $\delta\langle\hat{P}(t)\rangle \equiv$

$\langle\hat{P}(t)\rangle - \langle\hat{P}\rangle$. The Fourier transforms of the electric field and the polarization change are then given by

$$E(t) = \int_{-\infty}^{\infty} \frac{d\omega}{2\pi} E(\omega) e^{-i\omega t}, \quad (24)$$

$$\delta\langle\hat{P}(t)\rangle = \int_{-\infty}^{\infty} \frac{d\omega}{2\pi} \delta P(\omega) e^{-i\omega t}. \quad (25)$$

The linear response of the polarization to the electric field is summarized in the form $\delta P(\omega) = \epsilon^R(\omega)E(\omega)$ by linear response theory, where the dielectric function $\epsilon^R(\omega)$ is given by the Fourier transform of the retarded polarization correlation function $\epsilon^R(t) = i\Theta(t)\langle[\hat{P}(t), \hat{P}(0)]\rangle$. Here, $\hat{P}(t)$ denotes the time evolution of the polarization in the absence of the external field (in the Heisenberg picture). The dielectric function $\epsilon^R(\omega)$ can be calculated from the imaginary-time evolution of the polarization as follows

$$\epsilon^R(\omega) = \epsilon(i\omega_n \rightarrow \omega + i\delta), \quad (26)$$

$$\epsilon(i\omega_n) = \int_0^\beta d\tau \epsilon(\tau) e^{i\omega_n \tau}, \quad (27)$$

$$\epsilon(\tau) = \langle T_\tau \hat{P}(\tau) \hat{P}(0) \rangle. \quad (28)$$

Here, $\hat{P}(\tau)$ represents the imaginary-time evolution of the polarization in the absence of the external field, which can be expressed by replacing the charge density $\rho(s)$ in Eq. (21) with its imaginary-time evolution $\rho(s, \tau)$. Because the microwave absorption intensity is directly related to $\text{Im} \epsilon^R(\omega)$ through the fluctuation-dissipation theorem, we restrict our attention to this quantity in what follows.

From Eqs. (27) and (28), the response function in the Matsubara representation is calculated as

$$\epsilon(i\omega_n) = \int_0^L ds ds' y(s) y(s') S_{\rho\rho}(s, s', i\omega_n). \quad (29)$$

Here, $S_{\rho\rho}(s, s', i\omega_n)$ is given as the Fourier transform of the imaginary-time density-density correlation function of the edge state $S_{\rho\rho}(s, s', \tau) \equiv \langle T_\tau \rho(s, \tau) \rho(s', 0) \rangle$. The charge density $\rho(s, \tau)$ is rewritten with the bosonic field as $\rho(s, \tau) = (2\pi)^{-1} \partial_s \varphi(s, \tau)$. To evaluate $S_{\rho\rho}(s, s', \tau)$, we introduce a source term coupled to an external field $\eta(s, \tau)$ into the generating functional defined in the previous subsection II A, as follows:

$$Z[\eta] \propto \int \mathcal{D}\varphi \mathcal{D}\lambda \mathcal{D}\phi e^{-S_{\text{edge}}[\varphi] - S_{\text{tun}}[\varphi] - S_\lambda[\varphi, \lambda, \phi] - S_\eta[\varphi]}, \quad (30)$$

$$S_\eta[\varphi] = \frac{1}{2\pi} \int_0^\beta d\tau \int_0^L ds \eta(s, \tau) \partial_s \varphi(s, \tau). \quad (31)$$

The correlation function can be calculated directly from the generating functional $Z[\eta]$, introduced in Eq. (30), as

$$\begin{aligned} S_{\rho\rho}(s, s', \tau, \tau') &\equiv \frac{1}{4\pi^2} \langle T_\tau \partial_s \varphi(s, \tau) \partial_{s'} \varphi(s', \tau') \rangle \\ &= \frac{1}{Z[\eta]} \frac{\delta^2 Z[\eta]}{\delta \eta(s, \tau) \delta \eta(s', \tau')} \Big|_{\eta=0}. \end{aligned} \quad (32)$$

D. The response function in a circular droplet

By functional differentiation of the resulting generating functional, we can obtain the explicit expression for the density correlation function $S_{\rho\rho}(s, s', i\omega_n)$:

$$S_{\rho\rho}(s, s', i\omega_n) = S_{\rho\rho}^{(0)}(s, s', i\omega_n) + \beta\Phi(i\omega_n)A(s, s', i\omega_n), \quad (33)$$

where one has

$$S_{\rho\rho}^{(0)}(s, s', i\omega_n) = \frac{\nu}{2\pi L} \sum_{k \neq 0} \frac{k}{vk - i\omega_n} e^{ik(s-s')}, \quad (34)$$

$$\Phi(i\omega_n) = \frac{2}{\beta\Lambda_n} \left(-1 + \frac{\langle \phi_n \phi_{-n} \rangle}{2\beta\Lambda_n} \right), \quad (35)$$

$$A(s, s', i\omega_n) = \frac{\nu^2}{4L^2} \sum_{i,j=1}^2 (-1)^{i+j} \times \sum_{k,k' \neq 0} \frac{e^{ik(s-s_i)} e^{-ik'(s'-s_j)}}{vk - i\omega_n vk' - i\omega_n}. \quad (36)$$

In Eq. (35), we introduced the correlator for the local fields

$$\langle \phi_n \phi_{-n} \rangle = \frac{1}{Z[0]} \int \mathcal{D}\phi \phi_n \phi_{-n} e^{-S_0[\phi] - S_{\text{tun}}[\phi]}. \quad (37)$$

For details of the calculation, see Appendix B. Using the results of Eqs. (33)–(36), the integration in Eq. (29) yields the following response function in the Matsubara formalism

$$\epsilon(i\omega_n) = \epsilon_0(i\omega_n) + \delta\epsilon(i\omega_n), \quad (38a)$$

$$\epsilon_0(i\omega_n) = \frac{\nu L^2}{16\pi^2} \left[\frac{1}{\omega_T + i\omega_n} + \frac{1}{\omega_T - i\omega_n} \right], \quad (38b)$$

$$\delta\epsilon(i\omega_n) = \frac{\beta\nu^2 L^2}{16\pi^2} \Phi(i\omega_n) \left[\frac{1}{(\omega_T - i\omega_n)^2} + \frac{1}{(\omega_T + i\omega_n)^2} - \frac{\cos \frac{2\pi(s_1+s_2)}{L}}{\omega_T} \left(\frac{1}{\omega_T + i\omega_n} + \frac{1}{\omega_T - i\omega_n} \right) \right]. \quad (38c)$$

Here $\epsilon_0(i\omega_n)$ corresponds to the response function of the free droplet without a QPC, while $\delta\epsilon(i\omega_n)$ characterizes the modification of the response function due to the quasiparticle tunneling at a QPC. In the absence of QPC, $\delta\epsilon(i\omega_n)$ vanishes, and we see from the expression in Eq. (38b) that the resonance corresponds to a peak at frequency $\omega = \omega_T \equiv 2\pi\nu/L$, which is the characteristic frequency of the droplet. We notice that, in order to obtain Eq. (38c), we made the assumption $|s_1 - s_2| = L/2$.

In order to obtain the response function in the presence of tunneling at the QPC, one needs to evaluate the

bosonic correlator $\Phi(i\omega_n)$ [Eq. (35)]. This cannot be done exactly in the general case. In this work, we use two different methods to obtain $\Phi(i\omega_n)$ [and thus $\epsilon(i\omega_n)$]: on the one hand, we analytically calculate second-order perturbation in the tunneling strength V ; on the other hand, we use the numerical method of path integral Monte Carlo (PIMC) for arbitrary tunneling amplitudes. The PIMC method allows us not only to obtain results beyond the perturbative limit but also to confirm the perturbative results in their regime of validity.

From this point onward, and unless mentioned otherwise, we focus on a symmetric circular droplet, with a QPC connecting the positions $s_1 = 0$ and $s_2 = L/2$ (see Fig. 2).

E. Perturbation theory

When the tunneling strength V is small enough, it is possible to perform a perturbative expansion of the bosonic correlator $\Phi(i\omega_n)$ of Eq. (35). This leads to

$$\epsilon(i\omega_n) = \epsilon_0(i\omega_n) + V\epsilon^{(1)}(i\omega_n) + V^2\epsilon^{(2)}(i\omega_n) + O(V^3) \quad (39)$$

Since the zeroth-order response function ϵ_0 exhibits narrow resonance peaks at $\pm\omega_T$, quasiparticle tunneling at the QPC is expected to change both the resonance frequencies and the peak widths. However, a bare perturbative expansion of the form in Eq. (39) does not allow one to directly extract these quantities, since the peak positions and linewidths are determined by the zeros of the inverse response function rather than by additive corrections to $\epsilon(i\omega_n)$ itself. To properly characterize these effects, we therefore introduce the interaction kernel $\Gamma(i\omega_n)$ as follows

$$\Gamma(i\omega_n) \equiv \epsilon_0^{-1}(i\omega_n) - \epsilon^{-1}(i\omega_n). \quad (40)$$

Within this formulation, the real and imaginary parts of $\Gamma(\omega)$ directly encode the tunneling-induced peak shifts and the corresponding changes in the linewidth. This represents a significant methodological distinction from earlier analyses [45], which were based on bare first-order perturbative expansions of the response function and therefore did not capture the peak shifts. Another important difference from previous studies is that we include contributions up to second order in perturbation theory. When the analysis is restricted to first order, only the shift of the resonance peak can be captured, whereas changes in the linewidth emerge only starting from second order. By taking into account second-order contributions, it becomes possible to incorporate information that is intrinsic to fractional quantum Hall physics, such as the renormalization of the linewidth.

Using Eqs. (35), (38c) and (39), we obtain for $\Gamma(i\omega_n)$ up to second order in V :

$$\Gamma^{(2)}(i\omega_n) = -V \frac{64\pi^2}{L^2} e^{-\bar{\Lambda}} - V^2 \frac{32\pi^2 e^{-2\bar{\Lambda}}}{L^2} \left[8\nu \left(\frac{1}{\omega_T - i\omega_n} + \frac{1}{\omega_T + i\omega_n} \right) + \mathcal{P}_+(0) + \mathcal{P}_-(0) - \mathcal{P}_+(i\omega_n) + \mathcal{P}_-(i\omega_n) - 2\beta \right]. \quad (41)$$

Here, $\mathcal{P}_\pm(i\omega_n)$ and $\bar{\Lambda}$ are defined as

$$\mathcal{P}_\pm(i\omega_n) \equiv \int_0^\beta d\tau e^{i\omega_n \tau} e^{\pm \frac{2}{\beta} \sum_p \Lambda_p \cos \omega_p \tau}, \quad (42)$$

$$\bar{\Lambda} \equiv \frac{1}{\beta} \sum_{\omega_m} \Lambda_m, \quad (43)$$

and one can show that $e^{-\bar{\Lambda}} \simeq (\pi\alpha/L)^\nu$. Once $\Gamma^{(2)}$ is computed, the response function $\epsilon_p(i\omega_n)$ in the perturbative regime is then obtained as

$$\epsilon_p(i\omega_n) = \frac{1}{\epsilon_0^{-1}(i\omega_n) - \Gamma^{(2)}(i\omega_n)}. \quad (44)$$

After performing the analytic continuation to real frequency, the real part of $\Gamma^{(2)}(\omega + i\delta)$ corresponds to the shift in the position of the resonance peaks, while the imaginary part yields the broadening and deformation of the peaks. From Eq. (41), one readily sees that the first order term in $\Gamma^{(2)}(\omega + i\delta)$ is purely real, thus leading to a simple shift of the resonance peaks, while the second order term yields both a shift and a widening. Note that the order n term contains a factor $e^{-n\bar{\Lambda}} = (\pi\alpha/L)^{\nu n}$. As $(\pi\alpha/L) \ll 1$, this is a small factor that guarantees the validity of the perturbation expansion. As this factor increases when ν decreases, one can expect that higher-order terms in the perturbative expansion will be more important for a given V as ν decreases (see section IV).

F. Path Integral Monte-Carlo (PIMC) method

In this study, we also evaluate $\Phi(i\omega_n)$ using the path-integral Monte Carlo (PIMC) method and thereby obtain a numerically exact response function. In this approach, the partition function is represented by the imaginary path-integral of $\phi(\tau)$, and the representative paths contributing to the response functions are sampled according to the weight determined by the Euclidean action. From the $\Phi(i\omega_n)$ obtained via PIMC, we compute $\Gamma(i\omega_n)$ and perform numerical analytic continuation to finite real frequencies using the Padé approximation, thereby obtaining the response function on the real-frequency axis from Eq. (40). Since the PIMC results include higher-order effects in the coupling strength, this method enables us to access the response not only in the region dominated by second-order perturbations but also in regimes where higher-order effects become significant. The details of the PIMC method are presented in Appendix C.

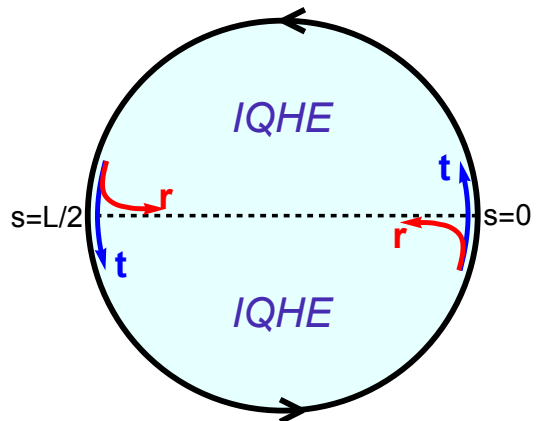


FIG. 3. Schematic and notation used in the exact IQHE calculation. The droplet is circular, with perimeter L . The quantum point contact connects the points at $s = 0$ and $s = L/2$, and is characterized by reflection and transmission amplitudes r and t .

III. RESULTS FOR THE IQH DROPLET CASE

In this section, we present the analytical calculation for the integer quantum Hall droplet with a filling factor $\nu = 1$, where the edge state is described by a non-interacting chiral electron system. We benchmark the consistency of the perturbative and PIMC results against the analytic solution.

We consider a finite edge state in an integer quantum Hall droplet, as illustrated in Fig. 3. At the quantum point contact, which connects the points $s = 0$ and $s = L/2$, electrons can either be transmitted or reflected to the opposite point. We define the S matrix at the QPC as

$$\hat{S} = \begin{pmatrix} t & -ir \\ -ir & t \end{pmatrix}, \quad (45)$$

where r and $t = \sqrt{1 - r^2}$ are the reflection and transmission amplitudes, respectively (see Fig. 3), which are determined from the quasiparticle tunneling λ_r (see Appendix D). We note that $t = 1$ corresponds to the absence of a quantum point contact ($\lambda_r = 0$). As mentioned in Sec. II A, a uniform magnetic field is applied to the droplet, and as electrons move along the edge, they acquire a phase factor $e^{i\phi_{\text{ABS}}/L}$ due to the Aharonov-Bohm

(AB) effect. The AB phase is given by $\phi_{AB} = 2\pi\Phi/\Phi_0$, as stated previously, where the flux quantum is $\Phi_0 = h/e$.

By imposing the twisted boundary conditions that account for the AB effect, the wavenumber is discretized as

$$k_{n,j} = \frac{4\pi}{L}(n + \delta_j), \quad (n \in \mathbb{Z}, j = 1, 2), \quad (46a)$$

$$\delta_1 = \frac{\chi}{2\pi} - \frac{\phi_{AB}}{4\pi}, \quad (46b)$$

$$\delta_2 = \frac{1}{2} - \frac{\chi}{2\pi} - \frac{\phi_{AB}}{4\pi}, \quad (46c)$$

where $\chi = \arctan(r/t) \in [0, \pi/2]$ denotes the coupling strength at the QPC (for a detailed derivation, see Appendix D). In the absence of the QPC ($r = 0$), the energy-level spacing is simply given by an integer multiple of $2\pi/L$, reflecting the edge-state length L . When introducing the QPC, the energy levels are divided into two groups $k_{n,1}$ and $k_{n,2}$, having their wavenumbers shifted in opposite directions by a factor $\chi/2\pi$. The AB phase ϕ_{AB} induces uniform shifts of both wavenumbers, $k_{n,1}$ and $k_{n,2}$, which have the same effect as changing the chemical potential.

The electrons that pass through the QPC at $s = L/2$ acquire $\Theta_j = (-1)^j\chi$ for the wavenumber $k_{n,j}$ (see Appendix D). Accordingly, the imaginary-time evolution of the electron field operator, $\psi(s, \tau)$, is expressed as

$$\psi(s, \tau) = \frac{1}{\sqrt{L}} \sum_n \sum_{j=1,2} e^{ik_{n,j}s - vk_{n,j}\tau} g_j(s) c_{n,j}, \quad (47)$$

$$g_j(s) = \begin{cases} 1, & (s < L/2), \\ e^{i\Theta_j}, & (s > L/2), \end{cases}. \quad (48)$$

The imaginary-time response function is given by

$$S_{\rho\rho}(s, s', \tau) = \langle \psi^\dagger(s, \tau) \psi(s', 0) \rangle \langle \psi(s, \tau) \psi^\dagger(s', 0) \rangle. \quad (49)$$

for $0 < \tau < \beta$. By substituting Eqs. (47)-(49) into Eq. (29) and performing the integration over s and s' , the imaginary part of the dielectric function is calculated as

$$\begin{aligned} \text{Im} \epsilon^R(\omega) &= \frac{L^2 \sin^2 \chi}{16\pi^3} \\ &\times \sum_{m,n} \frac{f(vk_{n,1}) - f(vk_{m,2})}{(n-m + \chi/\pi)^2 (n-m + \chi/\pi - 1)^2} \\ &\times \left[\delta(\omega + v(k_{n,1} - k_{m,2})) - \delta(\omega - v(k_{n,1} - k_{m,2})) \right]. \end{aligned} \quad (50)$$

The response function is determined by transitions between the different eigenstates with eigenenergies $vk_{n,1}$ and $vk_{m,2}$, as indicated by the delta function $\delta(\omega \pm v(k_{n,1} - k_{m,2}))$ (see also Fig. 11 in Appendix D). Due to the factor $f(vk_{n,1}) - f(vk_{m,2})$, only the transition from an unoccupied state to an occupied one is possible at zero temperature.

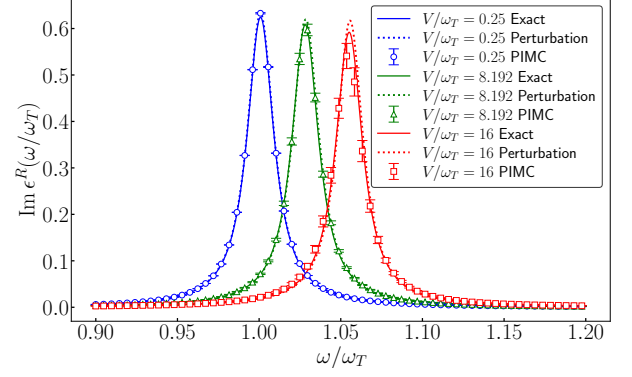


FIG. 4. Imaginary part of the dielectric function $\text{Im} \epsilon^R(\omega)$ for the $\nu = 1$ IQH droplet, shown in units of L^2/ω_T . The temperature is set to $T/\omega_T = 0.1$. Solid and dashed lines show the results of scattering theory [Eq. (50)] and second-order perturbation theory [Eqs. (41)-(44)], respectively, while symbols with error bars represent numerical data obtained using the PIMC method. Dimensionless coupling strengths are $V/\omega_T = 0.25, 8.192, \text{ and } 16$. For visual clarity, delta functions are broadened into Lorentzians with linewidth $\delta = \omega_T/100$.

This exact expression allows us to check the correctness of our two calculation methods: the second-order perturbation and the PIMC simulation. To make comparison easier, the delta function in Eq. (50) is replaced with a Lorentzian function with a small width δ . This corresponds to the analytic continuation $i\omega_n \rightarrow \omega + i\delta$ with a finite value of δ . Fig. 4 shows the response function $\text{Im} \epsilon^R(\omega)$ for the case of a circular droplet at $\nu = 1$. It compares the results of all three methods: the exact theoretical treatment of Eq. (50), the results obtained from the second-order perturbation theory [Eqs. (41)-(44)], and the numerical results computed using the PIMC method. In this comparison, a clear shift of the peak at $\omega = \omega_T = 2\pi v/L$ toward higher frequencies is observed as the coupling strength increases, and all three results show good overall agreement within the range of coupling strengths considered. For larger coupling strengths, particularly at $V/\omega_T = 16$, the Monte Carlo and exact theoretical results remain in good agreement, whereas the second-order perturbation begins to show a slight deviation in intensity. We found that the second-order perturbation agrees well with the exact theoretical treatment for moderate coupling strengths, while the PIMC simulations accurately reproduce the exact theoretical results over the entire range considered.

IV. RESULTS FOR THE FQH DROPLET CASE

Next, we discuss the behavior of $\text{Im} \epsilon^R(\omega)$ for a FQH droplet, based on perturbation theory and numerical cal-

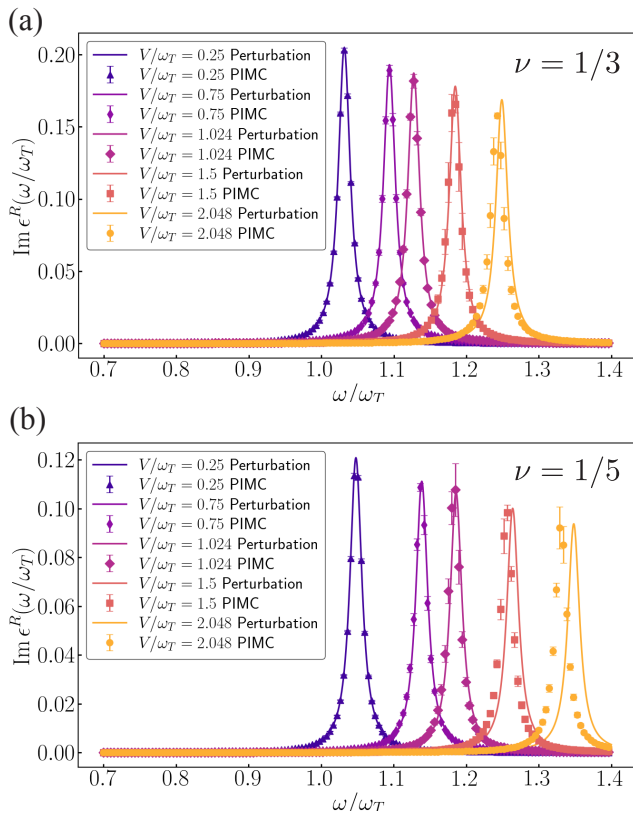


FIG. 5. Imaginary part of the dielectric function $\text{Im } \epsilon^R(\omega)$ for FQH droplets with (a) $\nu = 1/3$ and (b) $\nu = 1/5$ at temperature $T/\omega_T = 0.1$. Solid lines show results from second-order perturbation theory, whereas symbols with error bars represent data obtained using PIMC. Coupling strengths are $V/\omega_T = 0.25, 0.75, 1.024, 1.5,$ and 2.048 . A finite broadening $\delta = \omega_T/100$ is used.

calculations using the PIMC method, as an exact analytical calculation is not available in this case. Through this comparison, we further examine how the deviation between the perturbative and PIMC results depends on the filling factor.

Figs. 5(a) and 5(b) show the behavior of $\text{Im } \epsilon^R(\omega)$ for $\nu = 1/3$ and $1/5$, respectively, with varying dimensionless coupling strength $V/\omega_T = 0.25, 0.75, 1.024, 1.5,$ and 2.048 at a fixed temperature of $T/\omega_T = 0.1$. To make the peak shift clearer, we have used a finite broadening factor $\delta = \omega_T/100$ in the analytic continuation. The solid lines represent the perturbative results, while the plotted points denote the PIMC results. As in the case of the IQH droplet, the resonance peak shifts towards higher frequencies as the coupling strength increases. In both figures, this peak shift is more pronounced than in the IQH droplet. Moreover, for a given value of the coupling strength V , the shift is found to be larger for $\nu = 1/5$ than for $\nu = 1/3$. As seen from Eq. (41), the first and second order terms are accompanied by factors

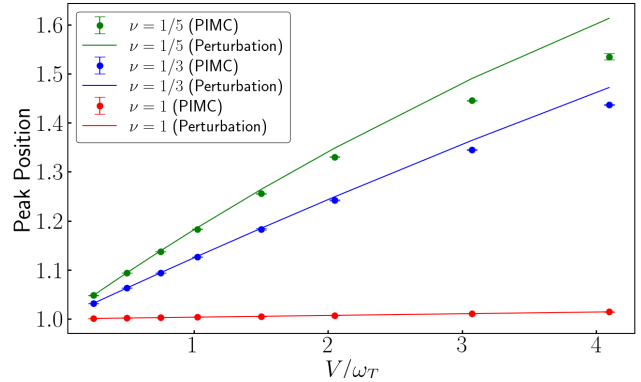


FIG. 6. Dependence of resonance-peak positions on tunneling strength for filling fractions $\nu = 1/5, 1/3,$ and 1 . Solid curves denote results from second-order perturbation theory, while symbols represent PIMC results.

of $e^{-\bar{\Lambda}}$ and $e^{-2\bar{\Lambda}}$, respectively. These factors get larger as ν decreases since $e^{-\bar{\Lambda}} \simeq (\pi\alpha/L)^\nu$. Therefore, it can be concluded that the effect of the coupling strength becomes more significant for smaller ν .

In Fig. 5, it can also be seen that as the coupling strength increases, a noticeable deviation between the PIMC and second-order perturbative results begins to appear. This deviation emerges at smaller coupling strengths for $\nu = 1/5$ than for $\nu = 1/3$, indicating that the $\nu = 1/5$ state is more sensitive to the coupling strength and exhibits higher-order effects more prominently. Fig. 6 shows the dependence of the peak position on the coupling strength for $\nu = 1, 1/3,$ and $1/5$. The solid lines represent the peak shifts obtained from the second-order perturbation results, while the plotted points correspond to those obtained from the PIMC calculations. Within the range of coupling strengths shown, the peak for $\nu = 1$ exhibits only a small shift, and the perturbative and PIMC results agree well. As discussed above, the peak shift becomes larger as ν decreases from $1/3$ to $1/5$. As the coupling strength increases, a noticeable deviation appears between the perturbative and PIMC results, with the deviation being more significant for $\nu = 1/5$ than for $\nu = 1/3$. This observation suggests that higher-order effects become increasingly important for smaller filling factors, and that such effects are successfully captured by the PIMC calculations.

Next, Figs. 7(a) and 7(b) show the temperature dependence of $\text{Im } \epsilon^R(\omega)$ for $\nu = 1/3$ and $\nu = 1/5$. The coupling strength is fixed at $V/\omega_T = 1.5$. As in Fig 5, the solid lines represent the perturbative results, while the plotted points denote the PIMC results. For both $\nu = 1/3$ and $\nu = 1/5$, the increase in linewidth with rising temperature is commonly observed in both the perturbative and PIMC results. In the present formulation, phonon effects are not taken into account, indicating that the linewidth broadening is caused by thermal fluctuations.

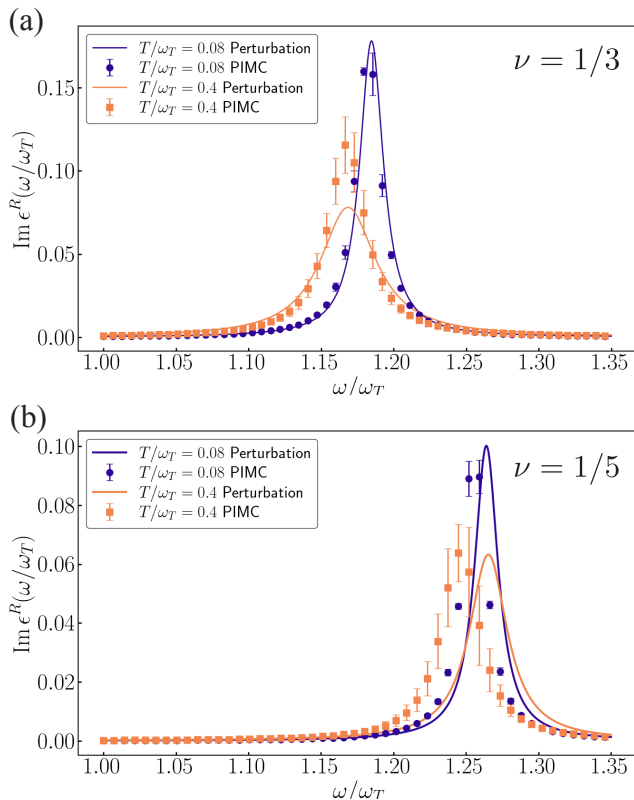


FIG. 7. Imaginary part of the dielectric function $\text{Im} \epsilon(\omega)$ at $T/\omega_T = 0.08$ (blue) and 0.4 (orange) for FQH droplets with (a) $\nu = 1/3$ and (b) $\nu = 1/5$ at coupling strength $V/\omega_T = 1.5$. A broadening factor $\delta = \omega_T/100$ is used.

In the PIMC results, a low-energy shift with increasing temperature is observed for both $\nu = 1/3$ and $\nu = 1/5$. While the perturbative result for $\nu = 1/3$ exhibits a similar behavior, the one for $\nu = 1/5$ shows no noticeable peak shift as the temperature increases. From this result, the low-energy peak shift observed for $\nu = 1/5$ is considered to be caused by higher-order effects.

V. RESULTS FOR THE REALISTIC GEOMETRY CASE

We now present the dielectric response in a more realistic geometry. So far, for simplicity, we have focused on a circular droplet geometry. In the following, we consider a geometry constructed from two overlapping circles of equal radius R , whose centers are laterally offset by $2a$, as illustrated in Fig. 8. Equation (29) provides the general expression for the response function, and by using the edge profile $y(s)$ corresponding to this droplet shape, the calculation can be carried out in the same manner as in the circular case. Importantly, the geometry dependence enters only through the edge profile $y(s)$, while the bosonic correlation function is geometry-

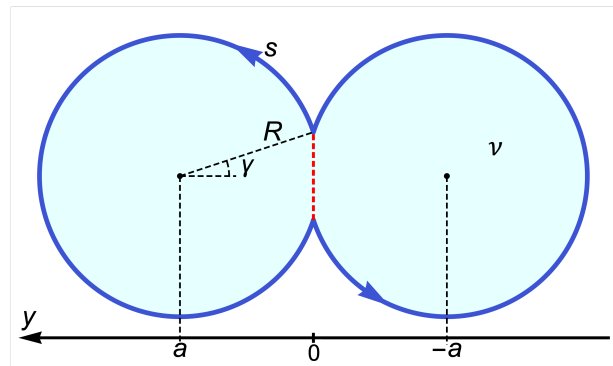


FIG. 8. Schematic of a realistic droplet geometry composed of two circular arcs joined at a junction. The QPC is formed by a constriction at this junction, whose opening angle is denoted by γ .

independent. Therefore, responses for different geometries can be obtained using a single set of Monte Carlo data for the bosonic correlator, without repeating the numerically expensive simulations.

In Fig. 8 the radius of each circle, R , is given by $R = L/[4(\pi - \gamma)]$, as obtained from the geometry shown in the figure. Furthermore, from the relation $R \cos \gamma = a$, it follows that the angle γ is determined once the distance between the centers of the two circles is specified. At this point, $y(s)$ can be expressed as follows:

$$y(s) = \begin{cases} R [\cos \gamma - \cos(R^{-1}s + \gamma)], & (s < L/2), \\ -R [\cos \gamma - \cos(R^{-1}s + 3\gamma)], & (s > L/2), \end{cases} \quad (51)$$

By performing the integration in Eq. (29), the response function in Matsubara space is obtained as follows:

$$\epsilon^{\text{real}}(i\omega_n) = \epsilon_0^{\text{real}}(i\omega_n) + \delta\epsilon^{\text{real}}(i\omega_n), \quad (52a)$$

$$\epsilon_0^{\text{real}}(i\omega_n) = \frac{8\nu R^{-2} \cos^2 \gamma}{\pi L} \times \sum_{l \in \mathbb{Z}} \frac{1}{\Delta_l (R^{-2} - \Delta_l^2)^2 (v\Delta_l - i\omega_n)}, \quad (52b)$$

$$\delta\epsilon^{\text{real}}(i\omega_n) = \frac{16\beta\nu^2 R^{-2} \cos^2 \gamma}{L^2} \Phi(i\omega_n) \times \left[\sum_{l \in \mathbb{Z}} \frac{1}{\Delta_l (R^{-2} - \Delta_l^2)^2 (v\Delta_l - i\omega_n)} \right]^2, \quad (52c)$$

where $\Delta_l \equiv 2(2l - 1)\pi/L$. The resulting dielectric function displays a set of peaks at energies set by $v\Delta_l$, with $l \in \mathbb{Z}$. Therefore, since $v\Delta_l = (2l - 1)\omega_T$, it follows that in the geometry shown in Fig. 8, multiple peaks appear at odd multiples of ω_T . This geometry reduces to that of the circular droplet with QPCs located at $s = 0$ and $s = L/2$ when $\gamma = \pi/2$. Indeed, Eqs. (52b) and (52c) coincide with Eqs. (38b) and (38c) in the limit $\gamma \rightarrow \pi/2$ for $s_1 + s_2 = L/2$.

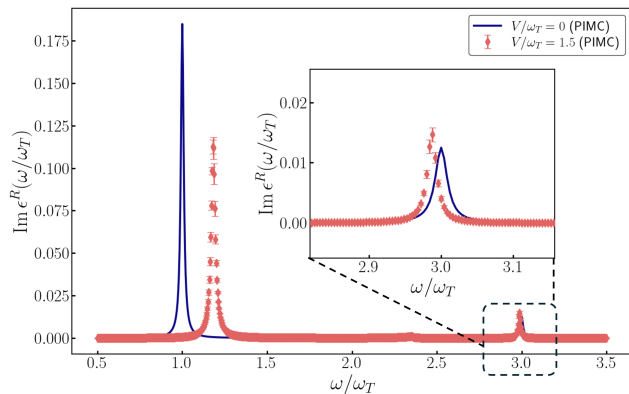


FIG. 9. Imaginary part of the dielectric function $\text{Im } \epsilon^R(\omega)$ at $T/\omega_T = 0.1$ for a $\nu = 1/3$ FQH droplet with the geometry shown in Fig. 8. The solid curve shows the analytical result at zero tunneling strength, $V/\omega_T = 0$, while symbols represent PIMC data at $V/\omega_T = 1.5$. The constriction of the droplet is controlled by the geometric angle γ , which is set to $\gamma = \pi/15$. A broadening $\delta = \omega_T/100$ is used. The inset shows a magnified view of the secondary peak.

Fig. 9 shows the calculated $\text{Im } \epsilon^R(\omega)$ for the $\nu = 1/3$ FQH droplet with the geometry illustrated in Fig. 8. It is confirmed that the secondary peak appears at three times the frequency of ω_T . As indicated from Eqs. (52b) and (52c), the amplitude decays rapidly when increasing the mode index l . In addition, as the coupling strength increases, a peak shift occurs, similar to the case of the circular droplet. The direction of the shift depends on the peak position. The peak located at $\omega/\omega_T = 1$ shifts toward higher frequencies, while the one at $\omega/\omega_T = 3$ shifts toward lower frequencies.

VI. SUMMARY

In this work, we investigated the microwave response of fractional quantum Hall (FQH) droplets containing a quantum point contact using a combination of path-integral Monte Carlo (PIMC) simulations and perturbation theory up to second order in the tunneling strength. For integer quantum Hall droplets, we benchmarked the approach against results obtained from quantum scattering theory, confirming the consistency of the response functions in regimes where analytical solutions are available.

We demonstrated that quasiparticle tunneling induces resonance peak shifts as well as thermal linewidth broadening, which were not addressed in the original proposal of Ref. [45]. We further showed that these peak shifts can be discussed reasonably only when the interaction kernel of the response function is taken into account, highlighting the limitations of bare perturbative expansions. The resulting behavior exhibits a clear dependence on the filling factor, reflecting the evolution of correlation strength

in FQH states and explaining the increasing deviation between PIMC and finite-order perturbative results at smaller filling factors.

Because the PIMC framework naturally incorporates higher-order contributions beyond perturbation theory while retaining geometric and thermal flexibility, it provides a robust tool for evaluating microwave response in regimes where perturbative approaches become inaccurate. These results establish microwave spectroscopy as a quantitative probe of quasiparticle dynamics and collective edge excitations in mesoscopic quantum Hall droplets, and offer a practical pathway for connecting theoretical modeling with experimental measurements across a wide range of filling factors and device geometries. Within the model considered here, quasiparticle (anyon) braiding effects are not the dominant mechanism influencing the microwave response. Extending the PIMC framework to regimes where braiding plays a central role in microwave resonances represents a promising direction for future investigation.

ACKNOWLEDGEMENTS

We thank G. Fève, G. Ménard and F. Parmentier for useful discussions on experimental aspects. F. M. is supported by the International Graduate Program of Innovation for Intelligent World (IIW) of the University of Tokyo. This research is supported by JST SPRING, Grant No. JPMJSP2108. T. K. acknowledges the support of the Japan Society for the Promotion of Science (JSPS KAKENHI Grant No. JP24K06951). F. M. and T. K. acknowledge the support of the Japan Science and Technology Agency (JST) ASPIRE Program No. JPM-JAP2410. This work was carried out in the framework of the project “ANY-HALL” (Grant No. ANR-21-CE30-0064-03). We acknowledge funding from the Agence Nationale de la Recherche under the France 2030 programme, reference ANR-22-PETQ-0012, and from the ERC advanced grant “ASTEC” (Grant No. 101096610). This French-Japanese collaboration is supported by the CNRS International Research Project “Excitations in Correlated Electron Systems driven in the GigaHertz range” (IRP ESEC).

Appendix A: Derivation of the effective action

In this appendix, we present the procedure for deriving the effective action. We first introduce the Fourier transforms of the bosonic field $\varphi(s, \tau)$ and the auxiliary field $\lambda(\tau)$ as

$$\varphi(s, \tau) = \frac{1}{L\beta} \sum_{k \neq 0} \sum_{\omega_n} \varphi_{k,n} e^{iks - i\omega_n \tau}, \quad (\text{A1})$$

$$\lambda(\tau) = \frac{1}{\beta} \sum_{\omega_n} \lambda_n e^{-i\omega_n \tau}. \quad (\text{A2})$$

Using these definitions, the imaginary-time actions $S_{\text{edge}}[\varphi]$ and $S_\lambda[\varphi, \lambda, \phi]$, originally defined in Eqs. (10) and (14), respectively, can be rewritten as

$$S_{\text{edge}}[\varphi] = \frac{1}{L\beta} \sum_{k \neq 0} \sum_{\omega_n} \frac{k(vk - i\omega_n)}{4\pi\nu} |\varphi_{k,n}|^2, \quad (\text{A3})$$

$$S_\lambda[\varphi, \lambda, \phi] = \frac{i}{L\beta} \sum_{k \neq 0} \sum_{\omega_n} \lambda_{-n} \times [(e^{iks_1} - e^{iks_2})\varphi_{k,n} - L\phi_n]. \quad (\text{A4})$$

Since the total action $S_{\text{edge}}[\varphi] + S_\lambda[\varphi, \lambda, \phi] + S_{\text{tun}}[\phi]$ is quadratic in $\varphi_{k,n}$, the bosonic field can be integrated out in the partition function defined in Eq. (13), yielding

$$Z \propto \int \mathcal{D}\lambda \mathcal{D}\phi e^{-S'_0[\phi, \lambda] - S_{\text{tun}}[\phi]}, \quad (\text{A5})$$

$$S'_0[\phi, \lambda] = \frac{\pi\nu}{L\beta} \sum_{k \neq 0} \sum_{\omega_n} \frac{|e^{iks_1} - e^{iks_2}|^2}{k(vk - i\omega_n)} |\lambda_n|^2 - \frac{i}{2\beta} \sum_{\omega_n} (\lambda_{-n}\phi_n + \lambda_n\phi_{-n}). \quad (\text{A6})$$

Because the effective action $S'_0[\phi, \lambda]$ is quadratic in λ_n , the auxiliary field λ_n can be further integrated out, leading to

$$Z \propto \int \mathcal{D}\phi e^{-S_0[\phi] - S_{\text{tun}}[\phi]}, \quad (\text{A7})$$

$$S_0[\phi] = \sum_{\omega_n} \frac{|\phi_n|^2}{4\beta\Lambda_n}. \quad (\text{A8})$$

Here, the coefficient Λ_n is given by

$$\Lambda_n = \frac{\pi\nu}{L} \sum_{k \neq 0} \frac{|e^{iks_1} - e^{iks_2}|^2}{k(vk - i\omega_n)}. \quad (\text{A9})$$

Noting that the summation over the wavenumber is taken for $k = 2\pi m/L$ with m being a nonzero integer, Λ_n can be evaluated as

$$\Lambda_n = \frac{\nu L}{\pi\nu} \sum_{m=1}^{\infty} \frac{1 - \cos 2\pi m(s_1 - s_2)/L}{m^2 + (\omega_n L/2\pi\nu)^2}. \quad (\text{A10})$$

Finally, by using the identity

$$\sum_{m=1}^{\infty} \frac{\cos nx}{n^2 + a^2} = \frac{\pi}{2a} \frac{\cosh a(\pi - x)}{\sinh a\pi} - \frac{1}{2a^2}, \quad (\text{A11})$$

valid for $0 \leq x \leq 2\pi$, we arrive at the expression given in Eq. (20).

Appendix B: Derivation of the density correlation function

In this appendix, we present the derivation of the density-density correlation function. As discussed in

Sec. II C, the charge density $\rho(s, \tau)$ can be expressed in terms of the bosonic field $\varphi(s, \tau)$ as

$$\begin{aligned} \rho(s, \tau) &= \frac{1}{2\pi} \partial_s \varphi(s, \tau) \\ &= \frac{1}{L\beta} \sum_{\omega_n} \sum_{k \neq 0} \frac{ik}{2\pi} \varphi_{k,n} e^{iks - i\omega_n \tau}. \end{aligned} \quad (\text{B1})$$

Accordingly, the density-density correlation function is written as

$$\begin{aligned} S_{\rho\rho}(s, s', \tau) &= \left(\frac{i}{2\pi L\beta} \right)^2 \sum_{\omega_n} \sum_{k, k' \neq 0} kk' \langle \varphi_{k,n} \varphi_{k', -n} \rangle \\ &\times e^{iks + ik's' - i\omega_n \tau}. \end{aligned} \quad (\text{B2})$$

The source term associated with the external field $\eta(s, \tau)$ in the action (31) can be rewritten, after Fourier transformation, as

$$S_\eta[\varphi] = \frac{1}{L\beta} \sum_{\omega_n} \sum_{k \neq 0} \frac{ik}{2\pi} \eta_{-k, -n} \varphi_{k,n}, \quad (\text{B3})$$

where $\eta_{-k, -n} = \eta_{k,n}^*$. From Eqs. (30) and (B3), we therefore obtain

$$\frac{1}{Z[0]} \frac{\delta^2 Z[\eta]}{\delta \eta_{-k, -n} \delta \eta_{-k', n}} \Big|_{\eta=0} = \left(\frac{i}{2\pi L\beta} \right)^2 kk' \langle \varphi_{k,n} \varphi_{k', -n} \rangle. \quad (\text{B4})$$

In complete analogy with the derivation of the effective action in Eq. (13), the fields $\varphi(s, \tau)$ and $\lambda(\tau)$ in the generating functional (30) can be integrated out by Gaussian integration, leaving only the local field degree of freedom $\phi(\tau)$. At this stage, the generating functional takes the form

$$Z[\eta] \propto \int \mathcal{D}\phi e^{-S_{\text{eff}}[\phi] - S_{\eta,1}[\phi, \eta] - S_{\eta,2}[\eta]}, \quad (\text{B5})$$

where

$$S_{\eta,1}[\phi, \eta] = - \sum_{\omega_n} \sum_{k \neq 0} \frac{\nu(e^{-iks_2} - e^{-iks_1})}{2i\beta L \Lambda_n (vk - i\omega_n)} \eta_{-k, -n} \phi_n, \quad (\text{B6})$$

$$\begin{aligned} S_{\eta,2}[\eta] &= - \frac{\nu}{4\pi\beta L} \sum_{\omega_n} \left(\sum_{k \neq 0} \frac{k}{vk - i\omega_n} |\eta_{k,n}|^2 \right. \\ &\quad \left. - \sum_{k, k' \neq 0} \frac{\nu(e^{-iks_1} - e^{-iks_2})(e^{ik's_1} - e^{ik's_2})}{\Lambda_n (vk - i\omega_n)(vk' - i\omega_n)} \eta_{k,n}^* \eta_{k', n} \right). \end{aligned} \quad (\text{B7})$$

Using Eqs. (B5)–(B7), we obtain

$$\begin{aligned} \frac{1}{Z[0]} \frac{\delta^2 Z[\eta]}{\delta \eta_{-k, -n} \delta \eta_{-k', n}} \Big|_{\eta=0} &= \left\langle \frac{\delta^2 e^{-S_{\eta,1}[\phi, \eta]}}{\delta \eta_{-k, -n} \delta \eta_{-k', n}} \right\rangle_{\eta=0} + \left\langle \frac{\delta^2 e^{-S_{\eta,2}[\eta]}}{\delta \eta_{-k, -n} \delta \eta_{-k', n}} \right\rangle_{\eta=0}, \end{aligned} \quad (\text{B8})$$

where $\langle \dots \rangle = Z[0]^{-1} \int \mathcal{D}\phi(\dots) e^{-S_{\text{eff}}[\phi]}$. Evaluating each term on the right-hand side of Eq. (B8), we find

$$\left\langle \frac{\delta^2 e^{-S_{\eta,1}[\phi,\eta]}}{\delta\eta_{-k,-n}\delta\eta_{-k',n}} \right\rangle_{\eta=0} = \frac{\langle \phi_n \phi_{-n} \rangle}{\beta^2 \Lambda_n^2} \tilde{A}(i\omega_n), \quad (\text{B9})$$

$$\left\langle \frac{\delta^2 e^{-S_{\eta,2}[\eta]}}{\delta\eta_{-k,-n}\delta\eta_{-k',n}} \right\rangle_{\eta=0} = -\frac{2\tilde{A}(i\omega_n)}{\beta\Lambda_n} + \frac{\nu k}{2\pi L\beta(vk - i\omega_n)} \delta_{k,-k'}. \quad (\text{B10})$$

Here, we have introduced

$$\tilde{A}(i\omega_n) \equiv \sum_{i,j=1}^2 \frac{\nu^2 (-1)^{i+j+1} e^{-iks_i - ik's_j}}{4\beta^2 L^2 \Lambda_n^2 (vk - i\omega_n)(vk' + i\omega_n)}. \quad (\text{B11})$$

Combining these results with Eqs. (B2) and (B4), the density-density correlation function is obtained as

$$S_{\rho\rho}(s, s', \tau) = \sum_{\omega_n} \frac{2e^{-i\omega_n\tau}}{\beta\Lambda_n} \left[-1 + \frac{\langle \phi_n \phi_{-n} \rangle}{2\beta\Lambda_n} \right] A(s, s', i\omega_n) + \frac{\nu}{2\pi\beta L} \sum_{\omega_n} \sum_{k \neq 0} \frac{k}{vk - i\omega_n} e^{ik(s-s') - i\omega_n\tau}. \quad (\text{B12})$$

The function $A(s, s', i\omega_n)$ is identical to that defined in Eq. (36). Finally, by performing a Fourier transform with respect to imaginary time, we recover the expressions given in Eqs. (33)-(35).

Appendix C: PIMC method

In the path-integral Monte Carlo (PIMC) method, the imaginary-time path $\phi(\tau)$ is sampled according to the Boltzmann weight $e^{-S_{\text{eff}}[\phi]}$, where $S_{\text{eff}}[\phi]$ denotes the effective action. For numerical implementation, the imaginary-time interval $[0, \beta]$ is discretized, and the path is represented as $\phi(\tau_l)$ ($l = 0, 1, 2, \dots, N-1$), with $\tau_l = l\Delta\tau$. Here, $\Delta\tau = \beta/N$ is the time step and N is the number of discretization points. With this discretization, the effective action is approximately written as

$$S_{\text{eff}}[\phi] = S_0[\phi] + S_{\text{tun}}[\phi], \quad (\text{C1})$$

$$S_0[\phi] = \sum_{n=-N/2+1}^{N/2} \frac{|\phi_n|^2}{4\beta\Lambda_n}, \quad (\text{C2})$$

$$S_{\text{tun}}[\phi] = -V\Delta\tau \sum_{l=0}^{N-1} \cos[\phi(\tau_l)]. \quad (\text{C3})$$

The Fourier transform defined in Eq. (19) is accordingly modified to

$$\phi(\tau_l) = \frac{1}{\beta} \sum_{n=-N/2+1}^{N/2} \phi_n e^{-i\omega_n\tau_l}. \quad (\text{C4})$$

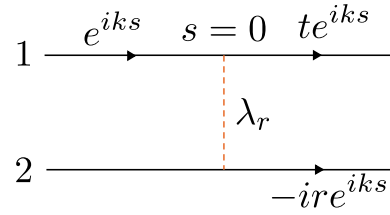


FIG. 10. Schematic for a wavefunction on two transmission channels for an electron incident from channel 1 toward the QPC.

Here, the Fourier components satisfy the relation $\phi_{-n} = \phi_n^*$. The Monte Carlo update procedure is implemented as follows. Starting from a given configuration $\{\phi_n\}$ in the frequency domain, we successively select a frequency index k in the range $[0, N/2]$ and propose a new value of ϕ_k drawn from the Gaussian distribution associated with the quadratic action $e^{-S_0[\phi]}$. The resulting configuration is denoted by $\{\phi_n\}^{(\text{new})}$. Both the original and the proposed configurations are then transformed back to the imaginary-time domain via the inverse Fourier transform, yielding $\{\phi(\tau_l)\}$ and $\{\phi(\tau_l)\}^{(\text{new})}$, respectively. Using these time-domain paths, we compute the change in the tunneling part of the action,

$$\Delta S = S_{\text{tun}}[\{\phi(\tau_l)\}^{(\text{new})}] - S_{\text{tun}}[\{\phi(\tau_l)\}]. \quad (\text{C5})$$

The proposed update is accepted with probability $\min(1, e^{-\Delta S})$, which is implemented by accepting the move if a uniform random number $r \in [0, 1)$ satisfies $r < e^{-\Delta S}$. A complete sweep over all frequency components constitutes one Monte Carlo step. By iterating this update procedure sufficiently many times, we generate representative imaginary-time paths distributed according to the weight $e^{-S[\phi(\tau_l)]}$. These sampled paths are subsequently used to evaluate correlation functions through the importance sampling technique.

Appendix D: Detailed calculations for IQH droplets

In this appendix, we present the derivation of the results for IQH droplets given in Sec. III. Throughout this appendix, we work in first quantization. In the absence of the QPC, the edge state of the IQH droplet is described by a noninteracting chiral electron channel, which satisfies the Schrödinger equation

$$-iv\partial_s\psi(s) = E\psi(s), \quad (0 \leq s < L). \quad (\text{D1})$$

To relate the strength of quasiparticle tunneling λ_r to the transmission and reflection amplitudes t and r , we introduce $\psi_1(s) = \psi(s)$ and $\psi_2(s) = \psi(s + L/2)$, both of which are discontinuous at $s = 0$ (see Fig. 10). In the limit $L \rightarrow \infty$, the Schrödinger equation in the presence of the QPC reads

$$\left(-iv\partial_s \hat{I} + \lambda_r \delta(s) \hat{\sigma}_x \right) \begin{pmatrix} \psi_1(s) \\ \psi_2(s) \end{pmatrix} = E \begin{pmatrix} \psi_1(s) \\ \psi_2(s) \end{pmatrix}. \quad (\text{D2})$$

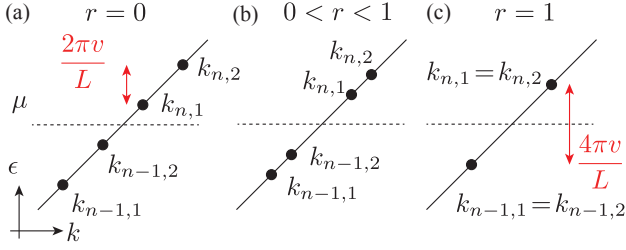


FIG. 11. Schematic of energy levels for (a) $r = 0$ ($\chi = 0$), (b) $0 < r < 1$ ($0 < \chi < \pi/2$), and (c) $r = 1$ ($\chi = \pi/2$). The horizontal axis represents the electron wave number, and the vertical axis the energy. The dashed line denotes the chemical potential.

Here, \hat{I} is the identity matrix, and $\hat{\sigma}_x$ is the x -component Pauli matrix. Consider the scattering ansatz

$$\psi_1(s) = \begin{cases} e^{iks}, & (s < 0), \\ te^{iks}, & (s > 0), \end{cases} \quad (\text{D3})$$

$$\psi_2(s) = \begin{cases} 0, & (s < 0), \\ -ir e^{iks}, & (s > 0). \end{cases} \quad (\text{D4})$$

Substituting Eqs. (D3) and (D4) into equation (D2) and integrating across $x = 0$ yields

$$t = \frac{1 - \lambda_r^2/4v^2}{1 + \lambda_r^2/4v^2}, \quad (\text{D5})$$

$$r = \frac{\lambda_r/v}{1 + \lambda_r^2/4v^2}. \quad (\text{D6})$$

Thus, $r > 0$ for $\lambda_r > 0$ ($\tilde{V} > 0$). In comparison with the PIMC simulation, the short-distance cutoff is identified as $\alpha = v\Delta\tau$ (see also Appendix C).

For a finite system, the eigenwavenumbers and eigenenergies are denoted by $k_{n,j}$ and $E_{n,j} = vk_{n,j}$, respectively. The wavefunction of the chiral edge mode takes the form

$$\psi(s) = \begin{cases} e^{iks+i\phi_{AB}s/L}, & (0 < s < L/2), \\ e^{iks+i\phi_{AB}s/L+i\Theta}, & (L/2 < s < L), \end{cases} \quad (\text{D7})$$

where Θ is a phase shift at the QPC and ϕ_{AB} is an Aharonov–Bohm phase induced by the external magnetic field. The normalization is set to unity since the energy eigenvalues do not depend on it. The incident and outgoing wavefunctions at the QPCs are given by

$$\psi_{\text{in}}(0) = \psi(L-0) = e^{ikL+i\phi_{AB}+i\Theta}, \quad (\text{D8})$$

$$\psi_{\text{out}}(0) = \psi(0+0) = 1, \quad (\text{D9})$$

$$\psi_{\text{in}}(L/2) = \psi(L/2-0) = e^{ikL/2+i\phi_{AB}/2}, \quad (\text{D10})$$

$$\psi_{\text{out}}(L/2) = \psi(L/2+0) = e^{ikL/2+i\phi_{AB}/2+i\Theta}. \quad (\text{D11})$$

Applying the S matrix in Eq. (45), we obtain

$$\begin{pmatrix} \psi_{\text{out}}(0) \\ \psi_{\text{out}}(L/2) \end{pmatrix} = \begin{pmatrix} t & -ir \\ -ir & t \end{pmatrix} \begin{pmatrix} \psi_{\text{in}}(0) \\ \psi_{\text{in}}(L/2) \end{pmatrix}. \quad (\text{D12})$$

Substituting Eqs. (D8)-(D11) and eliminating $e^{i\Theta}$, one obtains

$$x^2 - 2irx - 1 = 0, \quad (\text{D13})$$

where $x = e^{ikL/2+i\phi_{AB}/2}$. The solutions are $x = ir \pm t = e^{i\chi}, e^{i(\pi-\chi)}$, where $\tan \chi = r/t$ ($0 \leq \chi \leq \pi/2$). The wavenumbers are thus discretized as $k_{n,j} = 4\pi(n+\delta_j)/L$, where $\delta_1 = (2\chi - \phi_{AB})/4\pi$ and $\delta_2 = 1/2 - \delta_1$ denote the QPC-induced shifts. These satisfy $0 \leq \delta_1 \leq 1/4 \leq \delta_2 \leq 1/2$. Figure 11 shows a schematic energy diagram for $\phi_{AB} = -\pi$. In the absence of the QPC ($r = 0$), the wavenumber reduces to $k = 2\pi(m+1/2)/L$ as expected. On the other hand, for the decoupled droplets ($r = 1$), the wavenumber becomes doubly degenerate, as $k = 4\pi(n+1/2)/L$. The phase shifts follow from Eqs. (D8)-(D11) and are given by

$$\Theta_j = \begin{cases} -\chi, & (j = 1), \\ \chi, & (j = 2). \end{cases} \quad (\text{D14})$$

Using these eigenfunctions, the electron field operators are written as

$$\psi(x, \tau) = \frac{1}{\sqrt{L}} \sum_n \sum_{j=1,2} e^{ik_{n,j}x - vk_{n,j}\tau} g_j(x) c_{n,j}, \quad (\text{D15})$$

$$\psi^\dagger(x, \tau) = \frac{1}{\sqrt{L}} \sum_n \sum_{j=1,2} e^{-ik_{n,j}x + vk_{n,j}\tau} g_j^*(x) c_{n,j}^\dagger, \quad (\text{D16})$$

where $c_{n,j}$ ($c_{n,j}^\dagger$) denotes the annihilation (creation) operator and $g_j(x)$ is defined by

$$g_j(x) = \begin{cases} 1, & (x < L/2), \\ e^{i\Theta_j}, & (x > L/2). \end{cases} \quad (\text{D17})$$

Using the identity

$$y(x) = \frac{L}{2\pi} \sin \frac{2\pi x}{L} = \sum_{\eta=\pm 1} \frac{\eta L}{4\pi i} \exp\left(\frac{2\pi i \eta x}{L}\right), \quad (\text{D18})$$

the imaginary-time dielectric function reads

$$\begin{aligned} \epsilon(\tau) &= \frac{1}{L^2} \sum_{m,n} \sum_{j,j'=1}^2 e^{v(k_{n,j}-k_{m,j'})\tau} \\ &\quad \times f(vk_{n,j})(1-f(vk_{m,j'})) I_{n,j,m,j'} I_{n,j,m,j'}^*, \end{aligned} \quad (\text{D19})$$

where $f(\epsilon) = (e^{\beta\epsilon} + 1)^{-1}$ is the Fermi–Dirac distribution function and $I_{n,j,m,j'}$ is defined as

$$\begin{aligned} I_{n,j,m,j'} &= \frac{L}{4\pi i} \sum_{\eta=\pm 1} \int_0^L dx g_j^*(x) g_{j'}(x) \\ &\quad \times e^{2\pi i \eta x/L - i(k_{n,j}-k_{m,j'})x}. \end{aligned} \quad (\text{D20})$$

Carrying out the integration yields

$$I_{n,1,m,1} = I_{n,2,m,2} = 0, \quad (\text{D21})$$

$$I_{n,2,m,1} = \frac{iL^2 e^{i\chi} \sin \chi / 4\pi^2}{(m-n+\chi/\pi)(m-n-1+\chi/\pi)}, \quad (\text{D22})$$

$$I_{n,1,m,2} = -\frac{iL^2 e^{-i\chi} \sin \chi / 4\pi^2}{(n-m+\chi/\pi)(n-m-1+\chi/\pi)}. \quad (\text{D23})$$

After Fourier transformation and analytic continuation ($i\omega_n \rightarrow \omega + i\delta$), we obtain Eq. (50).

Appendix E: Detailed calculations of perturbation

Our starting point is the effective action derived in App. A. An auxiliary field $\xi(\tau) = \beta^{-1} \sum_n \xi_n e^{-i\omega_n \tau}$ is introduced. The generating functional then reads

$$Z[\xi] = \int \mathcal{D}\phi e^{-S_{\text{eff}}[\phi, \xi]}, \quad (\text{E1})$$

$$S_{\text{eff}}[\phi, \xi] = S_0[\phi] + S_{\text{tun}}[\phi] + \frac{1}{\beta} \sum_n \xi_{-n} \phi_n, \quad (\text{E2})$$

$$S_0[\phi] = \sum_n \frac{|\phi_n|^2}{4\beta\Lambda_n}, \quad (\text{E3})$$

$$S_{\text{tun}}[\phi] = -V \int d\tau \cos \phi(\tau). \quad (\text{E4})$$

The correlation function follows from functional differentiation

$$\langle \phi_n \phi_{-n} \rangle = \beta^2 \left. \frac{\delta^2 \log Z[\xi]}{\delta \xi_{-n} \delta \xi_n} \right|_{\xi=0}. \quad (\text{E5})$$

For $V = 0$,

$$Z_0[\xi] = \exp\left(\frac{1}{\beta} \sum_n \Lambda_n \xi_n \xi_{-n}\right), \quad (\text{E6})$$

yielding the non-interacting correlator

$$\langle \phi_n \phi_{-n} \rangle_0 = 2\beta\Lambda_n. \quad (\text{E7})$$

Expanding in S_{tun} ,

$$e^{-S_0 - S_{\text{tun}}} = e^{-S_0} \left(1 - S_{\text{tun}} + \frac{1}{2} S_{\text{tun}}^2 + \dots\right), \quad (\text{E8})$$

the first-order contribution to the generating functional reads

$$Z_1[\xi] = -V \int \mathcal{D}\phi \int d\tau \cos \phi e^{-S_0[\phi] - \beta^{-1} \sum_n \xi_{-n} \phi_n}. \quad (\text{E9})$$

Performing standard Gaussian integration of the ϕ field yields

$$\left. \frac{Z_1}{Z_0} \right|_{\xi=0} = -\beta V e^{-\bar{\Lambda}}, \quad (\text{E10})$$

$$\left. \frac{1}{Z_0} \frac{\delta^2 Z_1}{\delta \xi_{-n} \delta \xi_n} \right|_{\xi=0} = -2V e^{-\bar{\Lambda}} \Lambda_n \left(1 - \frac{2\Lambda_n}{\beta}\right), \quad (\text{E11})$$

with $\bar{\Lambda} = \beta^{-1} \sum_p \Lambda_p$. The first-order correction to the correlation function thus reads

$$\langle \phi_n \phi_{-n} \rangle_1 = 4\beta V \Lambda_n^2 e^{-\bar{\Lambda}}. \quad (\text{E12})$$

At second order, one has

$$Z_2[\xi] = \frac{V^2}{2} \int \mathcal{D}\phi \int d\tau d\tau' \cos \phi(\tau) \cos \phi(\tau') \times e^{-S_0[\phi] - \beta^{-1} \sum_n \xi_{-n} \phi_n}. \quad (\text{E13})$$

Again, performing the Gaussian integration over ϕ gives

$$\left. \frac{Z_2}{Z_0} \right|_{\xi=0} = +\frac{\beta V^2}{4} e^{-2\bar{\Lambda}} [\mathcal{P}_+(0) + \mathcal{P}_-(0)], \quad (\text{E14})$$

$$\begin{aligned} \left. \frac{1}{Z_0} \frac{\delta^2 Z_2}{\delta \xi_{-n} \delta \xi_n} \right|_{\xi=0} &= \frac{\Lambda_n V^2}{2} e^{-2\bar{\Lambda}} \\ &\times \left\{ \left(1 - \frac{4\Lambda_n}{\beta}\right) [\mathcal{P}_+(0) + \mathcal{P}_-(0)] \right. \\ &\left. + \frac{4\Lambda_n}{\beta} [\mathcal{P}_+(i\omega_n) - \mathcal{P}_-(i\omega_n)] \right\}, \quad (\text{E15}) \end{aligned}$$

where $\mathcal{P}_{\pm}(\omega_n)$ is defined in Eq. (42). The second-order correction to the correlation function becomes

$$\begin{aligned} \langle \phi_n \phi_{-n} \rangle_2 &= -2\beta V^2 \Lambda_n^2 e^{-2\bar{\Lambda}} \left[\mathcal{P}_+(0) + \mathcal{P}_-(0) \right. \\ &\left. - \mathcal{P}_+(i\omega_n) + \mathcal{P}_-(i\omega_n) - 2\beta \right]. \quad (\text{E16}) \end{aligned}$$

For $s_1 = 0$ and $s_2 = L/2$, the interaction kernel takes the form

$$\begin{aligned} \Gamma(i\omega_n) &= \frac{8\pi^2(\omega_T^2 + \omega_n^2)}{\nu L^2} \left[\frac{1}{\omega_T} \right. \\ &\left. - \frac{\omega_T^2 + \omega_n^2}{(\omega_T + \nu\beta\Phi)(\omega_T^2 + \omega_n^2) + \nu\beta\Phi(\omega_T^2 - \omega_n^2)} \right], \quad (\text{E17}) \end{aligned}$$

where $\Phi(i\omega_n)$ was defined in Eq. (35). Expanding in V , we are left with

$$\Gamma(i\omega_n) = \left. \frac{\partial \Gamma}{\partial V} \right|_{V=0} V + \frac{1}{2} \left. \frac{\partial^2 \Gamma}{\partial V^2} \right|_{V=0} V^2 + \mathcal{O}(V^3). \quad (\text{E18})$$

The coefficients of the expansion are then given by

$$\left. \frac{\partial \Gamma}{\partial V} \right|_{V=0} = \left. \frac{\partial \Gamma}{\partial \Phi} \frac{\partial \Phi}{\partial V} \right|_{V=0}, \quad (\text{E19})$$

$$\left. \frac{\partial^2 \Gamma}{\partial V^2} \right|_{V=0} = \left. \left(\frac{\partial^2 \Phi}{\partial V^2} \frac{\partial \Gamma}{\partial \Phi} + \left(\frac{\partial \Phi}{\partial V} \right)^2 \frac{\partial^2 \Gamma}{\partial \Phi^2} \right) \right|_{V=0}, \quad (\text{E20})$$

where the required derivatives read

$$\left. \frac{\partial \Gamma}{\partial \Phi} \right|_{V=0} = \frac{16\pi^2\beta}{L^2}, \quad (\text{E21})$$

$$\left. \frac{\partial^2 \Gamma}{\partial \Phi^2} \right|_{V=0} = -\frac{64\pi^2\nu\beta^2\omega_T}{L^2(\omega_T^2 + \omega_n^2)}, \quad (\text{E22})$$

$$\left. \frac{\partial \Phi}{\partial V} \right|_{V=0} = \frac{1}{\beta^2 \Lambda_n^2} \frac{\langle \phi_n \phi_{-n} \rangle_1}{V}, \quad (\text{E23})$$

$$\left. \frac{\partial^2 \Phi}{\partial V^2} \right|_{V=0} = \frac{2}{\beta^2 \Lambda_n^2} \frac{\langle \phi_n \phi_{-n} \rangle_2}{V^2}. \quad (\text{E24})$$

Substituting these back into Eq. (E18) and using Eqs. (E12) and (E16), reproduces the result of Eq. (41).

-
- [1] D. C. Tsui, H. L. Stormer, and A. C. Gossard, Two-dimensional magnetotransport in the extreme quantum limit, *Phys. Rev. Lett.* **48**, 1559 (1982).
- [2] R. B. Laughlin, Anomalous quantum hall effect: An incompressible quantum fluid with fractionally charged excitations, *Phys. Rev. Lett.* **50**, 1395 (1983).
- [3] B. I. Halperin, Quantized hall conductance, current-carrying edge states, and the existence of extended states in a two-dimensional disordered potential, *Phys. Rev. B* **25**, 2185 (1982).
- [4] L. Saminadayar, D. C. Glattli, Y. Jin, and B. Etienne, Observation of the $e/3$ Fractionally Charged Laughlin Quasiparticle, *Phys. Rev. Lett.* **79**, 2526 (1997).
- [5] R. de Picciotto, M. Reznikov, M. Heiblum, V. Umansky, G. Bunin, and D. Mahalu, Direct observation of a fractional charge, *Nature* **389**, 162 (1997).
- [6] F. Wilczek, Quantum mechanics of fractional-spin particles, *Phys. Rev. Lett.* **49**, 957 (1982).
- [7] D. Arovas, J. R. Schrieffer, and F. Wilczek, Fractional statistics and the quantum hall effect, *Phys. Rev. Lett.* **53**, 722 (1984).
- [8] C. Nayak, S. H. Simon, A. Stern, M. Freedman, and S. Das Sarma, Non-abelian anyons and topological quantum computation, *Rev. Mod. Phys.* **80**, 1083 (2008).
- [9] J. Nakamura, S. Liang, G. C. Gardner, and M. J. Manfra, Direct observation of anyonic braiding statistics, *Nat. Phys.* **16**, 931 (2020).
- [10] H. Bartolomei, M. Kumar, R. Bisognin, A. Marguerite, J.-M. Berroir, E. Bocquillon, B. Plaças, A. Cavanna, Q. Dong, U. Gennser, Y. Jin, and G. Fève, Fractional statistics in anyon collisions, *Science* **368**, 173 (2020).
- [11] J. Nakamura, S. Liang, G. C. Gardner, and M. J. Manfra, Fabry-Pérot Interferometry at the $\nu = 2/5$ Fractional Quantum Hall State, *Phys. Rev. X* **13**, 041012 (2023).
- [12] H. K. Kundu, S. Biswas, N. Ofek, V. Umansky, and M. Heiblum, Anyonic interference and braiding phase in a Mach-Zehnder interferometer, *Nat. Phys.* **19**, 515 (2023).
- [13] R. L. Willett, K. Shtengel, C. Nayak, L. N. Pfeiffer, Y. J. Chung, M. L. Peabody, K. W. Baldwin, and K. W. West, Interference Measurements of Non-Abelian $e/4$ & Abelian $e/2$ Quasiparticle Braiding, *Phys. Rev. X* **13**, 011028 (2023).
- [14] T. Werkmeister, J. R. Ehrets, Y. Ronen, M. E. Wesson, D. Najafabadi, Z. Wei, K. Watanabe, T. Taniguchi, D. E. Feldman, B. I. Halperin, A. Yacoby, and P. Kim, Strongly coupled edge states in a graphene quantum Hall interferometer, *Nat. Commun.* **15**, 6533 (2024).
- [15] T. Werkmeister, J. R. Ehrets, M. E. Wesson, D. H. Najafabadi, K. Watanabe, T. Taniguchi, B. I. Halperin, A. Yacoby, and P. Kim, Anyon braiding and telegraph noise in a graphene interferometer, *Science* **388**, 730 (2025).
- [16] B. Rosenow, I. P. Levkivskyi, and B. I. Halperin, Current correlations from a mesoscopic anyon collider, *Phys. Rev. Lett.* **116**, 156802 (2016).
- [17] C. Han, J. Park, Y. Gefen, and H. S. Sim, Topological vacuum bubbles by anyon braiding, *Nat. Commun.* **7**, 11131 (2016).
- [18] C. Mora, Anyonic exchange in a beam splitter (2022), [arXiv:2212.05123](https://arxiv.org/abs/2212.05123).
- [19] T. Morel, J.-Y. M. Lee, H.-S. Sim, and C. Mora, Fractionalization and anyonic statistics in the integer quantum hall collider, *Phys. Rev. B* **105**, 075433 (2022).
- [20] J.-Y. M. Lee and H. S. Sim, Non-Abelian anyon collider, *Nat. Commun.* **13**, 6660 (2022).
- [21] M. Ruelle, E. Frigerio, J.-M. Berroir, B. Plaças, J. Rech, A. Cavanna, U. Gennser, Y. Jin, and G. Fève, Comparing Fractional Quantum Hall Laughlin and Jain Topological Orders with the Anyon Collider, *Phys. Rev. X* **13**, 011031 (2023).
- [22] P. Glidic, O. Maillet, A. Aassime, C. Piquard, A. Cavanna, U. Gennser, Y. Jin, A. Anthore, and F. Pierre, Cross-Correlation Investigation of Anyon Statistics in the $\nu = 1/3$ and $2/5$ Fractional Quantum Hall States, *Phys. Rev. X* **13**, 011030 (2023).
- [23] T. Jonckheere, J. Rech, B. Grémaud, and T. Martin, Anyonic Statistics Revealed by the Hong-Ou-Mandel Dip for Fractional Excitations, *Phys. Rev. Lett.* **130**, 186203 (2023).
- [24] N. Schiller, Y. Shapira, A. Stern, and Y. Oreg, Anyon Statistics through Conductance Measurements of Time-Domain Interferometry, *Phys. Rev. Lett.* **131**, 186601 (2023).
- [25] J.-Y. M. Lee, C. Hong, T. Alkalay, N. Schiller, V. Umansky, M. Heiblum, Y. Oreg, and H. S. Sim, Partitioning of diluted anyons reveals their braiding statistics, *Nature* **617**, 277 (2023).
- [26] K. Iyer, F. Ronetti, B. Grémaud, T. Martin, J. Rech, and T. Jonckheere, Finite width of anyons changes their braiding signature, *Phys. Rev. Lett.* **132**, 216601 (2024).
- [27] M. Thamm and B. Rosenow, Effect of the soliton width on nonequilibrium exchange phases of anyons, *Phys. Rev. Lett.* **132**, 156501 (2024).
- [28] F. Ronetti, N. Demazure, J. Rech, T. Jonckheere, B. Grémaud, L. Raymond, M. Hashisaka, T. Kato, and T. Martin, Anyon braiding on the single edge of a fractional quantum hall state, *Phys. Rev. Lett.* **135**, 146601 (2025).
- [29] F. Ronetti, N. Demazure, J. Rech, T. Jonckheere, B. Grémaud, L. Raymond, M. Hashisaka, T. Kato, and T. Martin, Probing anyon statistics on a single-edge loop in the fractional quantum Hall regime, *Phys. Rev. B* **112**, 125166 (2025).
- [30] M. Ruelle, E. Frigerio, E. Baudin, J.-M. Berroir, B. Plaças, B. Grémaud, T. Jonckheere, T. Martin, J. Rech, A. Cavanna, U. Gennser, Y. Jin, G. Ménard, and G. Fève, Time-domain braiding of anyons, *Science* **389**, eadm7695 (2025).
- [31] H. Saleur, Edge states tunneling in the fractional quantum hall effect: integrability and transport, *Comptes Rendus Physique* **3**, 685 (2002).
- [32] D. C. Glattli, Tunneling experiments in the fractional quantum hall effect regime, in *The Quantum Hall Effect: Poincaré Seminar 2004*, edited by

- B. Douçot, V. Pasquier, B. Duplantier, and V. Rivasseau (Birkhäuser Basel, Basel, 2005) pp. 163–197.
- [33] V. Volkov and S. A. Mikhailov, Edge magnetoplasmons: low frequency weakly damped excitations in inhomogeneous two-dimensional electron systems, *Sov. Phys. JETP* **67**, 1639 (1988).
- [34] E. Andrei, D. Glattli, F. Williams, and M. Heiblum, Low frequency collective excitations in the quantum-hall system, *Surf. Sci.* **196**, 501 (1988).
- [35] V. Talyanskii, M. Wassermeier, A. Wixforth, J. Oshino, J. Kotthaus, I. Batov, G. Weimann, H. Nickel, and W. Schlapp, Edge magnetoplasmons in the quantum Hall effect regime, *Surf. Sci.* **229**, 40 (1990).
- [36] R. C. Ashoori, H. L. Stormer, L. N. Pfeiffer, K. W. Baldwin, and K. West, Edge magnetoplasmons in the time domain, *Phys. Rev. B* **45**, 3894 (1992).
- [37] N. B. Zhitenev, R. J. Haug, K. v. Klitzing, and K. Eberl, Experimental determination of the dispersion of edge magnetoplasmons confined in edge channels, *Phys. Rev. B* **49**, 7809 (1994).
- [38] N. Kumada, H. Kamata, and T. Fujisawa, Edge magnetoplasmon transport in gated and ungated quantum hall systems, *Physical Review B—Condensed Matter and Materials Physics* **84**, 045314 (2011).
- [39] I. Petković, F. Williams, K. Bennaceur, F. Portier, P. Roche, and D. C. Glattli, Carrier Drift Velocity and Edge Magnetoplasmons in Graphene, *Phys. Rev. Lett.* **110**, 016801 (2013).
- [40] M. Hashisaka, H. Kamata, N. Kumada, K. Washio, R. Murata, K. Muraki, and T. Fujisawa, Distributed-element circuit model of edge magnetoplasmon transport, *Phys. Rev. B* **88**, 235409 (2013).
- [41] N. Kumada, P. Roulleau, B. Roche, M. Hashisaka, H. Hibino, I. Petković, and D. Glattli, Resonant Edge Magnetoplasmons and Their Decay in Graphene, *Phys. Rev. Lett.* **113**, 266601 (2014).
- [42] A. C. Mahoney, J. I. Colless, S. J. Pauka, J. M. Hornibrook, J. D. Watson, G. C. Gardner, M. J. Manfra, A. C. Doherty, and D. J. Reilly, On-chip microwave quantum hall circulator, *Phys. Rev. X* **7**, 011007 (2017).
- [43] A. Endo, K. Koike, S. Katsumoto, and Y. Iye, Frequencies of the Edge-Magnetoplasmon Excitations in Gated Quantum Hall Edges, *J. Phys. Soc. Jpn.* **87**, 064709 (2018).
- [44] E. Frigerio, G. Rebola, M. Ruelle, H. Souquet-Basiège, Y. Jin, U. Gennser, A. Cavanna, B. Plaçais, E. Baudin, J.-M. Berroir, I. Safi, P. Degiovanni, G. Fève, and G. C. Ménard, Gate tunable edge magnetoplasmon resonators, *Commun. Phys.* **7**, 314 (2024).
- [45] J. Cano, A. Doherty, C. Nayak, D. Reilly, Microwave absorption by a mesoscopic quantum Hall droplet, *Phys. Rev. B* **88**, 165305 (2013).
- [46] B. Oblak, B. Lapierre, P. Moosavi, J.-M. Stéphan, and B. Estienne, Anisotropic Quantum Hall Droplets, *Phys. Rev. X* **14**, 011030 (2024).
- [47] C. L. Kane and M. P. A. Fisher, Contacts and edge-state equilibration in the fractional quantum hall effect, *Phys. Rev. B* **52**, 17393 (1995).
- [48] E. V. Deviatov, A. A. Kapustin, V. T. Dolgoplov, A. Lorke, D. Reuter, and A. D. Wieck, Equilibration between edge states in the fractional quantum hall effect regime at high imbalances, *Phys. Rev. B* **74**, 073303 (2006).
- [49] D. B. Mast, A. J. Dahm, and A. L. Fetter, Observation of Bulk and Edge Magnetoplasmons in a Two-Dimensional Electron Fluid, *Phys. Rev. Lett.* **54**, 1706 (1985).
- [50] D. C. Glattli, E. Y. Andrei, G. Deville, J. Poitrenaud, and F. I. B. Williams, Dynamical Hall Effect in a Two-Dimensional Classical Plasma, *Phys. Rev. Lett.* **54**, 1710 (1985).
- [51] A. M. Chang, Chiral Luttinger liquids at the fractional quantum Hall edge, *Rev. Mod. Phys.* **75**, 1449 (2003).
- [52] X.-G. Wen, Theory of the Edge States in Fractional Quantum Hall Effects, *Int. J. Mod. Phys. B* **06**, 1711 (1992).
- [53] M. R. Geller, D. Loss, Aharonov-Bohm effect in the chiral Luttinger liquid, *Phys. Rev. B* **56**, 9692 (1997).
- [54] J. von Delft and H. Schoeller, Bosonization for beginners — refermionization for experts, *Ann. Phys. (Berlin)* **510**, 225 (1998).
- [55] D. Loss, Parity effects in a Luttinger liquid: Diamagnetic and paramagnetic ground states, *Phys. Rev. Lett.* **69**, 343 (1992).
- [56] W. Magnus, On the exponential solution of differential equations for a linear operator, *Commun. Pure Appl. Math.* **7**, 649 (1954).
- [57] K. Moon, H. Yi, C. L. Kane, S. M. Girvin, and M. P. A. Fisher, Resonant Tunneling between Quantum Hall Edge States, *Phys. Rev. Lett.* **71**, 4381 (1993).